

1 **Improved Snow Property Retrievals by Solving for Topography in the Inversion of At-**
2 **sensor Radiance Measurements**

3
4 Brenton A. Wilder¹, Joachim Meyer¹, Josh Enterkine¹, Nancy F. Glenn^{1*}

5 ¹Department of Geosciences, Boise State University, Boise, ID, USA

6
7 Correspondence to: Nancy F. Glenn (nancyglenn@boisestate.edu)

8
9 **Abstract**

10 Accurately modelling optical snow properties like snow albedo and specific surface
11 area (SSA) are essential for monitoring the cryosphere in a changing climate and are
12 parameters that inform hydrologic and climate models. These snow surface properties can be
13 modelled from spaceborne imaging spectroscopy measurements but rely on Digital Elevation
14 Models (DEMs) of relatively coarse spatial scales (e.g. Copernicus at 30 m), which degrade
15 accuracy due to errors in derived products – such as slope and aspect. In addition, snow
16 deposition and redistribution can change the apparent topography and thereby static DEMs
17 may not be considered coincident with the imaging spectroscopy dataset. Testing in three
18 different snow climates (tundra, maritime, alpine), we established a new method that
19 simultaneously solves snow, atmospheric, and terrain parameters, enabling a solution that is

20 more unified across sensors and introduces fewer sources of uncertainty. We leveraged
21 imaging spectroscopy data from AVIRIS-NG and PRISMA (collected within 1 hour) to
22 validate this method and showed a 25% increase in performance for the radiance-based
23 method over the static method when estimating SSA. This concept can be implemented in
24 missions such as Surface Biology and Geology (SBG), Environmental Mapping and Analysis
25 Program (EnMap), and Copernicus Hyperspectral Imaging Mission for the Environment
26 (CHIME).

27

28 **Key Words:** Imaging Spectroscopy, Snow Properties, Topography, Snow Albedo

29

30 **1 Introduction**

31 Accurately mapping snow surface properties is essential for seasonal snow zones in a
32 changing climate especially in regions where seasonal snowpack is expected to change
33 dramatically in the coming decades (Siirila-Woodburn et al., 2021). For example, snow
34 albedo plays a crucial role in melting of the snowpack during the ablation season (Wang et
35 al., 2020) with changes in snow albedo directly affecting the amount of absorbed solar
36 radiation, and therefore the amount of snow that is melted off. Throughout the winter season,
37 snow albedo fluctuates due in part to grain size (Seidel et al., 2016) and light absorbing
38 particles (Kaspari et al., 2015; McKenzie, 2020; Schmale et al., 2017; Skiles & Painter,

39 2017). With a limited number of *in situ* snow stations around the globe, and the snow surface
40 constantly undergoing metamorphism across space and time, satellite imagery represents the
41 best potential for spatially and temporally complete mapping of snow properties. Accurately
42 retrieving snow albedo and other snow surface properties from satellite imagery is
43 paramount, especially in a rapidly changing climate (Malmros et al., 2018).

44 Retrieval of snow properties from satellite remote sensing relies on Digital Elevation
45 Models (DEMs) to correct for local terrain effects (Bair et al., 2021; Bair et al., 2022; Dozier
46 et al., 2022). In a previous study, researchers found global DEM products to have “blunders
47 and errors” when compared to airborne lidar, particularly in derived slope and aspect which
48 cause severe errors in calculated cosine of local solar illumination angles (μ_s) (Dozier et al.,
49 2022). They found errors in μ_s ranging from 0.048 to 0.117 (dimensionless) across several
50 sites for Copernicus global DEMs caused by errors in slope and aspect. The μ_s term is a
51 function (Eq. 1) of slope angle (S), slope azimuth angle or aspect (A), solar zenith angle (θ_0),
52 and solar azimuth angle (ϕ_0) – with the last two being well constrained:

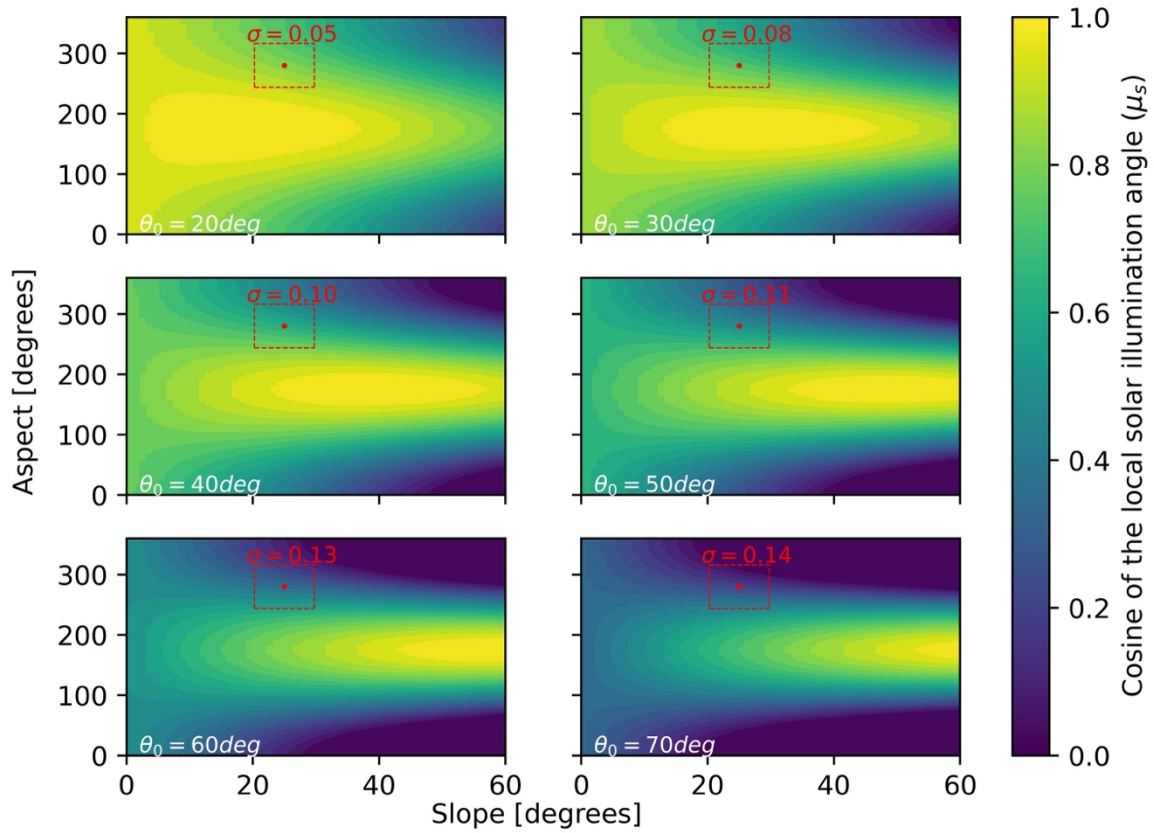
53

$$54 \quad \mu_s = \max[0, \cos(\theta_0) \cos(S) + \sin(\theta_0) \sin(S) \cos(\phi_0 - A)] \quad (1)$$

55

56 Because θ_0 and ϕ_0 are calculable with low errors, the biggest contribution to errors in μ_s
57 stem from slope and aspect. Errors in μ_s increase monotonically with increasing θ_0 (e.g., sun

58 setting has high θ_0 , as does solar noon in high latitude winters). This phenomenon can be
59 explained by plotting Eq. 1 for various θ_0 (Figure 1). Put simply, at higher θ_0 there is a
60 higher standard deviation in μ_s surrounding a known slope and aspect (with some temporally
61 consistent uncertainty), increasing the probability and magnitude of such an error. If one were
62 to compute standard deviations of μ_s across varying θ_0 , one would arrive at similar errors of
63 μ_s presented in Dozier et al. (2022). For clarity, in Figure 1 we have highlighted an example
64 case with slope= $25^\circ \pm 4.73$ and aspect= $280^\circ \pm 36.3$. Example uncertainties for this
65 exercise can be found in Table 2 of Dozier et al. (2022).



66

67 **Figure 1.** Cosine of local illumination angles (μ_s) as a function of slope (x-axis) and aspect
68 (y-axis) incremented by 1° , illustrating the problem at higher latitude, and/or winter
69 acquisitions, where standard deviation (σ) of μ_s increases monotonically with solar zenith
70 angles (θ_0). Aspect is shown here measured clockwise from north (with north containing a
71 discontinuity at 360 degrees). For this illustration ϕ_0 is fixed at a value of 175° . The red dots
72 represent the example point at slope= $25^\circ \pm 4.73$ and aspect= $280^\circ \pm 36.3$ and are bordered
73 by their uncertainty and the resulting σ .

74

75

76

77

78

79

80

81

82

83

84

85

86

87

88

89

90

91

92

Recent work has shown μ_s can be modelled using an optimal estimation framework given the Top of Atmosphere (TOA) radiance observed from imaging spectroscopy (Carmon et al., 2023). The authors solve for surface, atmospheric, and topographic state variables simultaneously in their model. This works physically because the partition of direct to diffuse light introduces a shape and magnitude effect on the TOA radiance spectra. However, retrieving snow optical properties is sensitive to directional reflectance which is significantly influenced by the viewing geometry and surface roughness (Bair et al., 2022), leading to possible shortcomings in this method specifically for snow covered pixels. To address this and expand upon this framework, we present a new method to account for terrain in snow covered areas. Our method was tested on pixels with greater than 75% snow cover in three different snow climates (tundra, maritime, and alpine) with spaceborne imaging spectroscopy with the aim to reduce error in derived snow properties by optimally solving for topography. The spaceborne results are validated against high confidence airborne spectrometer data. This work directly contributes to snow property retrievals in steep terrain and/or at times of high solar zenith angles for satellite imaging spectroscopy missions such as Surface Biology and Geology (SBG) (Cawse-Nicholson et al., 2021), Copernicus Hyperspectral Imaging Mission for the Environment (CHIME) (Celesti et al., 2022), and EnMap (Guanter et al., 2015).

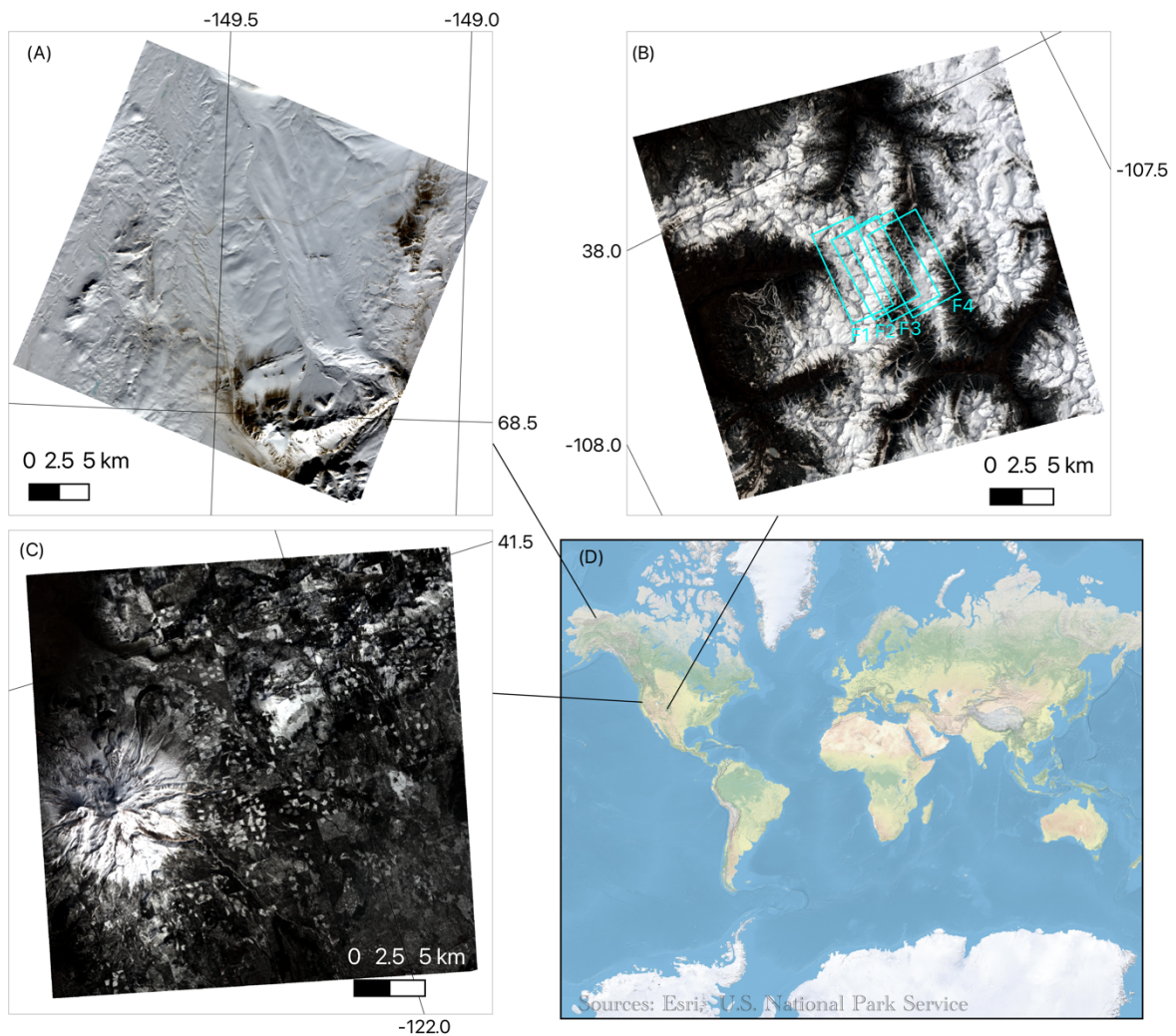
93 **2 Methods**

94 **2.1 Study area**

95 For our study, we used *PR*ecursore *I*perSpettrale della *M*issione *A*pplicativa
96 (PRISMA) imagery over three sites capturing different snow climates and solar zenith angles:
97 San Juan Mountains (Colorado, USA, 29 April 2021, $\theta_0=27^\circ$), Mount Shasta (California,
98 USA, 28 February 2021, $\theta_0=52^\circ$), and the Toolik area (Alaska, USA, 21 March 2021,
99 $\theta_0=68^\circ$) (Figure 2). The San Juan Mountains location is considered a high alpine site located
100 in interior continental USA with an elevation range of 2208-4129 m. The Mount Shasta site is
101 a maritime snow climate along the western coast of USA with an elevation range of 750-4232
102 m. The Toolik site (elevation range = 504-1748 m) is a high-latitude tundra site, being mostly
103 flat but with steep sections along the Brooks Range (along the southern part of the image).
104 PRISMA, launched by the Italian Space Agency (ASI) and beginning operation on March 22,
105 2019, is a spaceborne imaging spectroscopy mission collecting radiance at 30 m spatial
106 resolution across 239 bands spanning 400-2500 nm at a spectral resolution better than 12 nm
107 across the visible-near and shortwave infrared (Cogliati et al., 2021).

108 To validate our method, we used four existing Airborne Visible Infrared Imaging
109 Spectrometer-Next Generation (AVIRIS-NG) flightlines over the San Juan Mountains from
110 29 April 2021 (flying 1 hour after PRISMA acquisition). AVIRIS-NG collects radiance
111 measurements at variable spatial resolution (depending on the flight altitude) across 425

112 bands spanning 380-2510 nm in 5nm intervals (Green et al., 2023). For this flight, data were
113 collected at 4 m spatial resolution. We downloaded AVIRIS-NG apparent reflectance from
114 National Snow and Ice Data Center (NSIDC) and observation geometry data from NASA
115 Search Earth Data (Skiles & Vuyovich, 2023).



117 **Figure 2.** PRISMA true colour images for Toolik on 21 March 2021 (A), San Juan
118 Mountains on 29 April 2021 (B), and Mount Shasta on 28 February 2021 (C). Four
119 coincident AVIRIS-NG flightlines (F1-F4) are shown in cyan over the San Juan Mountains.

120

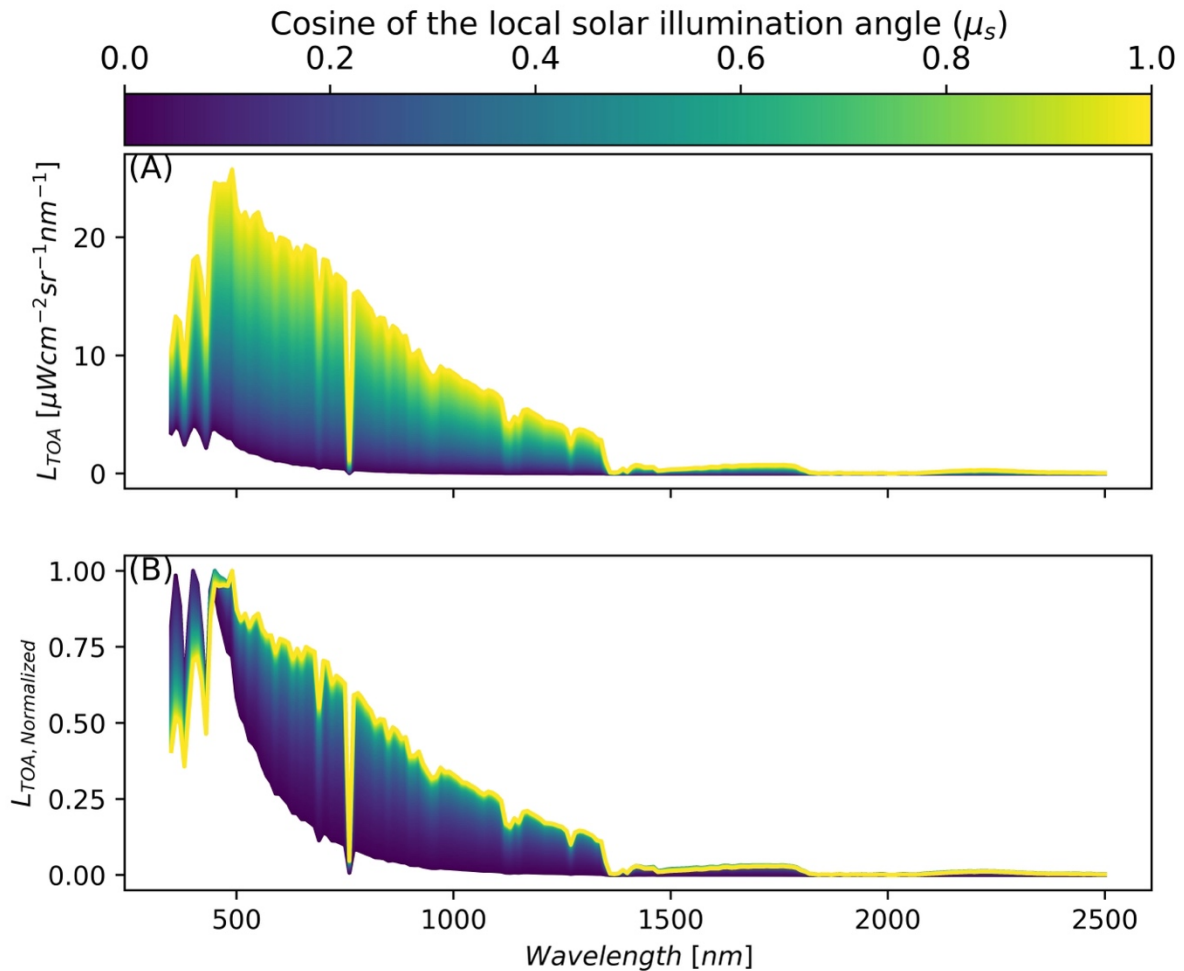
121 **2.2 Modelling surface, atmosphere, and topography from PRISMA**

122 The algorithmic improvements build off a workflow that estimates snow properties
123 given PRISMA TOA radiance, titled Global Optical Snow properties via High-speed
124 Algorithm using K-means (GOSHAWK) (Wilder et al., 2024). In short, our method uses the
125 analytic asymptotic radiative transfer model (AART) (Kokhanovsky & Zege, 2004) coupled
126 with libRadtran (Mayer & Kylling, 2005) to invert snow surface and atmospheric properties
127 (Bohn et al., 2021; Dalcin & Fang, 2021), and fractional covers of mixed pixels under varied
128 lighting conditions using non-linear numerical optimization (Bair et al., 2021). The
129 parameters solved for in the optimization routine include fractional covers, specific surface
130 area (SSA), light absorbing particle concentration (modelled as dust), liquid water
131 percentage, dimensionless aerosol optical depth at 550nm, and columnar water vapor in the
132 atmosphere. Here, we expand upon the algorithm considering recent work showing the
133 capacity to estimate μ_s from TOA radiance (Carmon et al., 2023; Bohn et al. 2024). This idea
134 is demonstrated in Figure 3 using fixed snow properties via AART and fixed atmosphere
135 properties via libRadtran across the range of plausible μ_s (i.e. 0 to 1). Like the findings in

136 Carmon et al. (2023), Figure 3 shows that μ_s controls both the spectral shape and magnitude
137 of observed TOA radiance with the effect varying across wavelengths. The greatest shape
138 effect can be seen in the visible spectrum (roughly 400-700 nm) due to the magnitude of the
139 diffuse irradiance. In combination with the magnitude and shape shift, this parameter
140 becomes solvable during optimization due to its strong separability – especially when
141 considering the entire spectrum data from a hyperspectral remote sensing source such as
142 PRISMA. It is important to note that μ_s impacts both the AART estimation of snow
143 reflectance and libRadtran estimation of incoming solar irradiance.

144

145



146

147 **Figure 3.** Synthetic data showing change in magnitude (A) and shape (B) of top of
 148 atmosphere radiance (L_{TOA}) with respect to changing local solar illumination angle (μ_s) for
 149 fixed snow surface state variables modelled with AART, and fixed atmospheric state
 150 variables modelled with libRadtran (viewing geometry was fixed as well). State variables and
 151 solar/view geometry were based on a PRISMA acquisition over southern Idaho on 8

152 December 2022. Figure (B) shows normalized radiance with respect to peak TOA radiance
153 across wavelengths to highlight the change in shape.

154

155 However, if we were only to optimize μ_s , the other key terms, local viewer zenith
156 angle (μ_v) and local phase angle (ξ) in the AART formulation for bidirectional reflectance of
157 snow (Eq. 2) (Kokhanovsky & Zege, 2004; Kokhanovsky et al., 2021a) would remain
158 constant from the available DEM (i.e., μ_s, μ_v, ξ are all derived from DEM),

159

$$160 \quad r_{snow}(\mu_s, \mu_v, \xi, \lambda) = r_0(\mu_s, \mu_v, \xi) \alpha_{snow}(\lambda)^f \quad (2)$$

161

162 where r_0 is the reflection function of a semi-infinite non-absorbing snow layer (Tedesco &
163 Kokhanovsky, 2007), α_{snow} is the spherical albedo [plane albedo can be computed using (26)
164 in Kokhanovsky et al. (2021a)], f is the escape function (Kokhanovsky et al., 2021a), and
165 r_{snow} is the bidirectional reflectance of snow. Keeping other terms μ_v and ξ the same are
166 problematic because snow reflectance is poorly approximated as a non-Lambertian surface
167 (Leroux & Fily, 1988), and the outcome will be greatly influenced by μ_v and ξ . Therefore, to
168 incorporate solving for μ_s, μ_v , and ξ from TOA radiance into the algorithm, we instead elect
169 to optimally solve for $\cos(\text{aspect})$ (i.e., “northness”) and $\sin(\text{aspect})$ (i.e., “eastness”) (Table
170 1).

171

172 **Table 1.** Parameter space and initial vectors used in numerical optimization for PRISMA

173 data.

Parameter [unit]	Definition	Feasible Range	Initial State	Type
f_{snow} [%]	Fractional snow in the mixed pixel	[0, 100]	10	Surface
f_{shade} [%]	Fractional shade in the mixed pixel	[0, 100]	20	Surface
f_{LC1} [%]	Fractional cover of endmember 1 (based on land cover value at pixel)	[0, 100]	50	Surface
f_{LC2} [%]	Fractional cover of endmember 2 (based on land cover value at pixel)	[0, 100]	20	Surface
SSA [$\text{m}^2 \text{kg}^{-1}$]	Specific surface area (SSA)	[2, 156]	40	Surface
LAP [$\mu\text{g g}^{-1}$]	Concentration of light absorbing particles, LAP, modelled as dust (PM-2.5).	[0, 145]	0	Surface
Liquid water [%]	Percentage of liquid water on the snow surface	[0, 50]	2	Surface
AOD 550 [%]	Dimensionless Aerosol Optical Depth (AOD) at 550 nm	[1,100]	10	Atmospheric
H_2O [mm]	Columnar water vapor in the atmosphere	[1,50]	1	Atmospheric
Eastness	$\sin(\text{aspect})$	[-1,1]	Variable	Topographic
Northness	$\cos(\text{aspect})$	[-1,1]	Variable	Topographic

174

175 Aspect can be solved during optimization by using the atan2 function. We chose to use this

176 method because eastness and northness are continuously differentiable, and therefore, are

177 suited for numerical optimization methods, whereas aspect is discontinuous at north (using

178 the convention of 0 and 360 degrees as north). We then can use this optimal aspect to
179 estimate μ_s (Eq. 1), μ_v , and ξ . This directly impacts Eq.2 and Eq. 5 (formulation of incoming
180 solar energy in the model) (Picard et al., 2020),

181

$$182 \quad E(\lambda) = \psi\mu_s E(\lambda)_{dir} + V_\Omega E(\lambda)_{diff} + \left[\left(1 + \frac{\cos(S)}{2} - V_\Omega \right) r(\lambda)_{surf} E(\lambda)_{diff} \right] \quad (5)$$

183

184 where E is total incoming irradiance, ψ is binary shade or no shade, E_{dir} and E_{diff} are the
185 direct and diffuse irradiance, respectively, V_Ω is the sky view factor (Dozier, 2022), and r_{surf}
186 is the reflectance of nearby terrain (which is assumed to be equal to the pixel itself). The term
187 E is solved within our non-linear numerical optimization method as described in Wilder et al.
188 (2024). This was modelled incorrectly in Wilder et al. (2024); however, this was corrected in
189 this paper where only diffuse irradiance is used in the 3rd term in Eq. 5. Also, adding in the
190 two extra parameters (eastness and northness) in our updated optimization scheme did not
191 change our run time significantly. Caution is advised against solving for slope *and* aspect in
192 the inversion due to the non-unique solution space (Figure 1); however, only considering
193 aspect ensures unique solutions of aspect, μ_s , μ_v , and ξ . We chose aspect because of its
194 greater impact on determining partition of direct and diffuse illumination and has been found
195 to be more impactful to errors associated with snow property retrieval (Donahue et al., 2023).
196 In this study we used estimate of total ozone column as input into creating the libRadtran

197 look up table specific for each image. We used the average weekly ozone over the bounds of
198 the image from Sentinel-5P NRTI O3: Near Real-Time Ozone dataset. This approach serves
199 an improvement over Wilder et al. (2024), where ozone was fixed at 300 Dobson Units.

200

201 **2.3 Estimating snow properties from AVIRIS-NG for validation**

202 Due to the fine signal to noise ratio and spatial resolution of AVIRIS-NG, we treated
203 the dataset as the ground reference. It also captured a similar spectral range to PRISMA
204 which made it a suitable comparison dataset. The main assumption here is that AVIRIS-NG
205 pixels at 4 m are relatively homogenous and are either snow or no-snow – which may not
206 always be the case. This could be a potential source of uncertainty in our analysis. To select
207 snow-covered pixels, we solved for NDSI (Normalized Difference Snow Index) using bands
208 at 600 nm and 1500 nm. We limited our retrieval of snow properties for NDSI greater than or
209 equal to 0.90 (Painter et al., 2013). A common approach to retrieve snow grain size from pure
210 snow pixels is to apply the scaled band area algorithm (Nolin & Dozier, 2000); however, it is
211 recognized that the large presence of liquid water is a limitation. The maximum air
212 temperature of 10.8° C on the day of the image at the San Juan Mountains site indicated that
213 elevated liquid water at the surface was probable (Center for Snow and Avalanche Studies,
214 2023). Additionally, reflectance spectra appeared to be shifted along the x-axis (wavelength)
215 due to the presence of liquid water. Therefore, we used constrained non-linear numerical

216 optimization to model apparent snow reflectance with AART by allowing fractional snow,
217 fractional shade, liquid water, and SSA to vary. We did not include rock or forest
218 endmembers in this formulation, assuming the 4 m pixels are relatively homogenous as
219 previously stated. Topographic incident angles were held constant based on the 4 m
220 resolution DEM provided by AVIRIS-NG. We minimized Root Mean Square Error (RMSE)
221 between observed-apparent and modelled-apparent snow reflectance from AART
222 wavelengths in the range, 1000-1250 nm. This range has high ice absorption and limited
223 impacts from atmospheric interference and LAP (Miller et al., 2016). The presence of liquid
224 water was included in our analysis by means of the composite refractive index of water and
225 ice (Donahue et al., 2022; Hale & Querry, 1973; Warren & Brandt, 2008). We assumed
226 similar grain shape assumptions for both PRISMA and AVIRIS-NG, and that if there is a bias
227 due to this it should be consistent between the two datasets in our analysis.

228

229 **2.4 Comparing modelled snow properties**

230 The algorithm was used in two different modes: 1) static topography based on the
231 Copernicus DEM (hereon called “*static*”); and 2) solved topography based on the algorithm
232 updates (hereon called “*radiance*”). To compare the accuracy of PRISMA derived SSA and
233 liquid water, we resampled the AVIRIS-NG optical property results (SSA and LWC) to
234 match the PRISMA resolution (30 m) and extents by using bilinear interpolation. Then, we

235 sampled all valid pixels where PRISMA and AVIRIS-NG had snow. We then computed r-
236 pearson correlation coefficient, Mean Bias, and RMSE for the radiance and static methods
237 (with respect to AVIRIS-NG). Finally, we used Copernicus derived slope and aspect maps to
238 determine where the largest errors were occurring on the landscape to compare with the
239 theoretical basis presented in Figure 1. We do this by using the mean absolute difference with
240 respect to μ_s . We expected to see higher differences in north facing aspects (i.e., μ_s
241 approaches 0), and where θ_0 was higher. To test the interaction with θ_0 more fully, we
242 extended the analysis to Mount Shasta, CA, and Toolik, Alaska, where no *in situ data*
243 existed. We compared the modelled properties between the radiance and static methods to
244 assess how these assumptions impacted results for these types of data at 30 m scale.

245

246 **2.5 Comparing DEM and radiance derived μ_s**

247 To ensure the resulting radiance derived μ_s were valid we downloaded the best
248 available validation data sources for comparison. For the San Juan and Shasta sites, we
249 collected DEM products at 1 m spatial resolution and collected 5 m spatial resolution DEM
250 for the Toolik site (U.S. Geological Survey, 2019; U.S. Geological Survey, 2022). Then, we
251 computed slope, aspect, solar zenith angle, and solar azimuth angle for all pixels to compute
252 μ_s at the native resolution (Eq. 1). Then, we used bilinear interpolation to resample the 1 m
253 and 5 m products to 30 m to exactly match the extents and resolution of our PRISMA images.

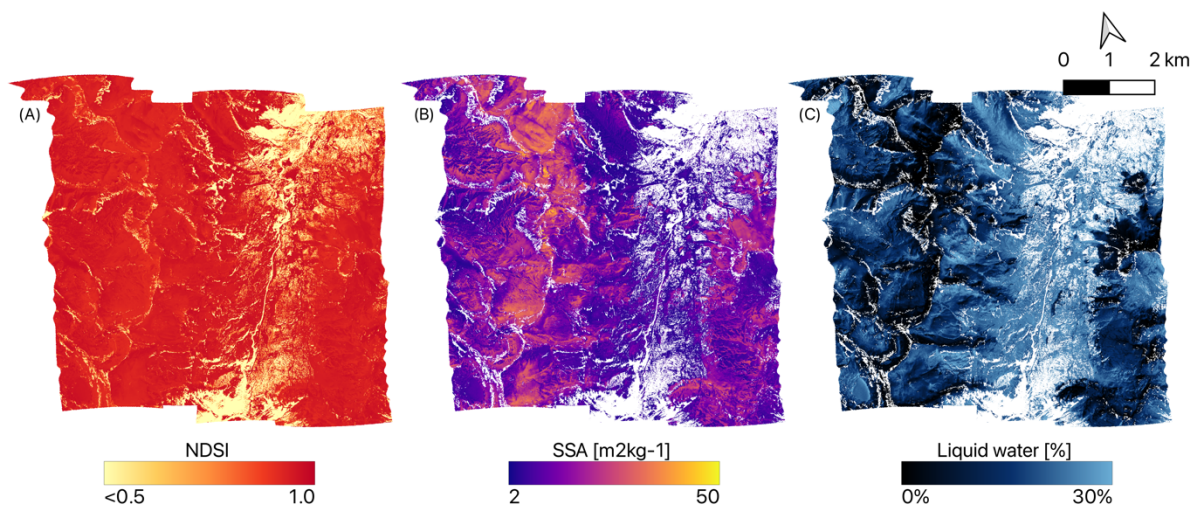
254 We would like to acknowledge that while these are the best freely available datasets for our
255 images, they still do not capture the true snow-on topography, and instead are a
256 representation of the “snow-free” surface. We compared matching pixels to determine
257 RMSE, R^2 , and Mean Bias. Pixels that were marked as shadow from ray tracing were
258 excluded from this comparison.

259

260 **3 Results**

261 **3.1 Validation using AVIRIS-NG data over the San Juan Mountains**

262 Over the area of the flightlines, AVIRIS-NG estimated mean SSA = $18.0 \pm 8.3 \text{ m}^2 \text{ kg}^{-1}$
263 ¹, PRISMA radiance method estimated mean SSA = $19.6 \pm 5.8 \text{ m}^2 \text{ kg}^{-1}$, and PRISMA static
264 method estimated mean SSA = $22.0 \pm 12.1 \text{ m}^2 \text{ kg}^{-1}$. When comparing the SSA performance
265 over each pixel to the AVIRIS-NG flightlines (Figure 4) we found the PRISMA radiance
266 method ($r=0.43$; $\text{RMSD}=8.0 \text{ m}^2 \text{ kg}^{-1}$; $\text{bias}=+1.7 \text{ m}^2 \text{ kg}^{-1}$; $n=36,412$) performed slightly better
267 than the static method ($r=0.23$; $\text{RMSD}=13.6 \text{ m}^2 \text{ kg}^{-1}$; $\text{bias}=+4.0 \text{ m}^2 \text{ kg}^{-1}$; $n=36,412$) for SSA.



268

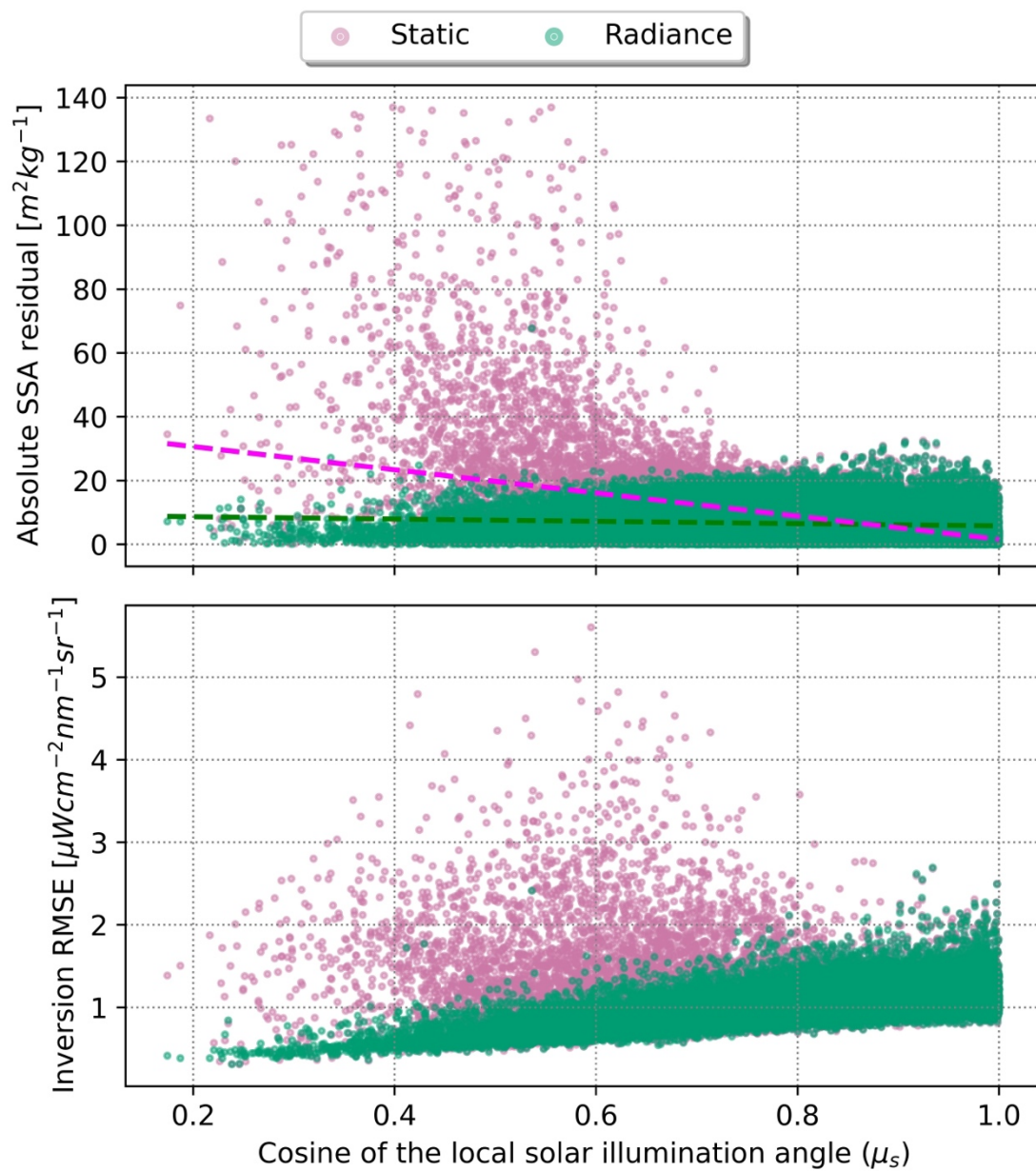
269 **Figure 4.** Snow properties computed from AVIRIS-NG (4 m spatial resolution) on 29 April
 270 2021 including NDSI (A), SSA (B), and LWC (C) for the San Juan Mountains site.

271

272 There was not a significant improvement in liquid water estimation between radiance ($r=0.67$;
 273 RMSD=10%; bias=-8%; $n=36,412$) and static ($r=0.67$; RMSD=10%; bias=-9%; $n=36,412$).
 274 Furthermore, it appeared that there was a consistent liquid water bias of 8 to 9%, hinting that
 275 more melt had occurred during the AVIRIS-NG flights. As previously noted, the temperatures
 276 were well above freezing during the overpass of AVIRIS-NG and occurred roughly 1 hour later
 277 in the day compared to the PRISMA acquisition. This most likely explains the higher liquid
 278 water and lower SSA observed by AVIRIS-NG. We further tested this by masking out areas
 279 where AVIRIS-NG liquid water content was greater than 0.1%, to establish areas where low
 280 amounts of melt occurred between the two acquisitions. We found that performance of

281 PRISMA static (RMSD=14.2 m² kg⁻¹; rRMSD=49%; n=181) and radiance (RMSD=6.9 m² kg⁻
282 ¹; rRMSD=23%; n=181) methods were more accurate for these areas. The radiance method
283 performed slightly better, suggesting a modest 25% improvement in accuracy for SSA over the
284 static method when considering pixels that were less impacted by melt.

285 Additionally, comparing all pixels we found improvement from radiance occurred
286 mostly on steep, north facing aspects (e.g., when μ_s approached 0). We found the absolute
287 residual increased as μ_s approached zero for the static method ($r = -0.47$; $p < 0.01$), while this
288 relationship was diminished nearly by a factor of 5 for the radiance method ($r = -0.10$; $p < 0.01$)
289 (Figure 5.A). These errors were caused by incorrect terrain information in the inversion, where
290 inversion error increased proportionately in the static method (Figure 5.B).



291

292 **Figure 5.** Absolute difference in modelled SSA when compared to AVIRIS-NG for radiance

293 method (green) and static method (pink) respect to μ_s (A) and resulting RMSE from the

294 inversion from PRISMA with respect to μ_s (B). Error in the static method increases
295 significantly when μ_s approached zero ($r = -0.47$; $p < 0.01$); however, the difference was less
296 noticeable in the radiance method ($r = -0.10$; $p < 0.01$).

297

298 **3.2 Comparing radiance and static methods between sites**

299 On average across each of the images, radiance and static methods provided similar
300 retrieved parameters within less than one standard deviation (Table 2). In general, this means
301 there is not a significant difference at the 30 m scale for computing parameters such as SSA
302 and broadband albedo (BA) when considering the entire image. Interestingly when terrain is
303 fixed, the static model compensated for incorrect illumination by increasing the aerosol optical
304 depth (thereby reducing the amount of direct solar radiation). Investigating the errors more
305 closely, we found much larger differences in retrieved properties where μ_s approached 0
306 (Figure 6). The difference in distributions matched closely to the theoretical demonstration
307 (Figure 1) and is most likely associated with the standard error of slope and aspect from
308 Copernicus DEM given the illumination conditions. This result also demonstrates the
309 difference between the two methods had the biggest impact for images where θ_0 was high,
310 resulting in potentially inaccurate retrievals that impact both surface and atmospheric state
311 variables on relatively mild slopes.

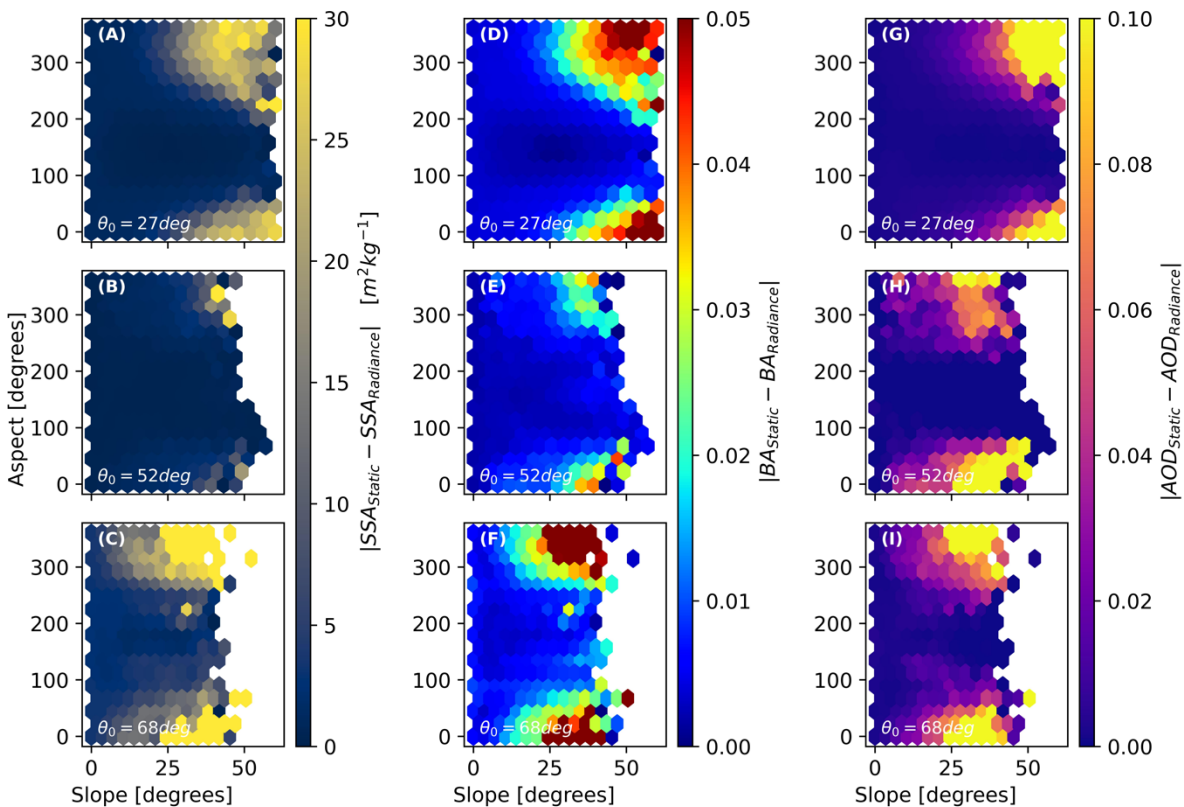
312

313 **Table 2.** Image-wide statistics comparing derived properties between the two methods (static
 314 vs. radiance) processing the PRISMA imagery for all three sites.

Site	PRISMA Method	Mean SSA [m ² kg ⁻¹]	Mean Broadband Albedo	Mean Liquid water [%]	Mean AOD at 550 nm	Mean water column vapour [mm]
San	Static	23.3 +/- 14.9	0.79 +/- 0.03	3.5 +/- 4.8	0.05 +/- 0.13	6.7 +/- 1.1
Juan	Radiance	19.6 +/- 5.9	0.78 +/- 0.03	3.9 +/- 5.0	0.01 +/- 0.01	6.8 +/- 0.3
Shasta	Static	11.0 +/- 6.0	0.77 +/- 0.04	1.6 +/- 3.3	0.04 +/- 0.10	7.6 +/- 1.3
	Radiance	10.7 +/- 6.2	0.77 +/- 0.05	1.9 +/- 3.8	0.01 +/- 0.04	7.7 +/- 1.1
Toolik	Static	30.1 +/- 9.6	0.85 +/- 0.02	0.0 +/- 0.0	0.02 +/- 0.03	1.0 +/- 0.4
	Radiance	27.7 +/- 7.9	0.84 +/- 0.02	0.0 +/- 0.0	0.01 +/- 0.01	1.0 +/- 0.2

315

316



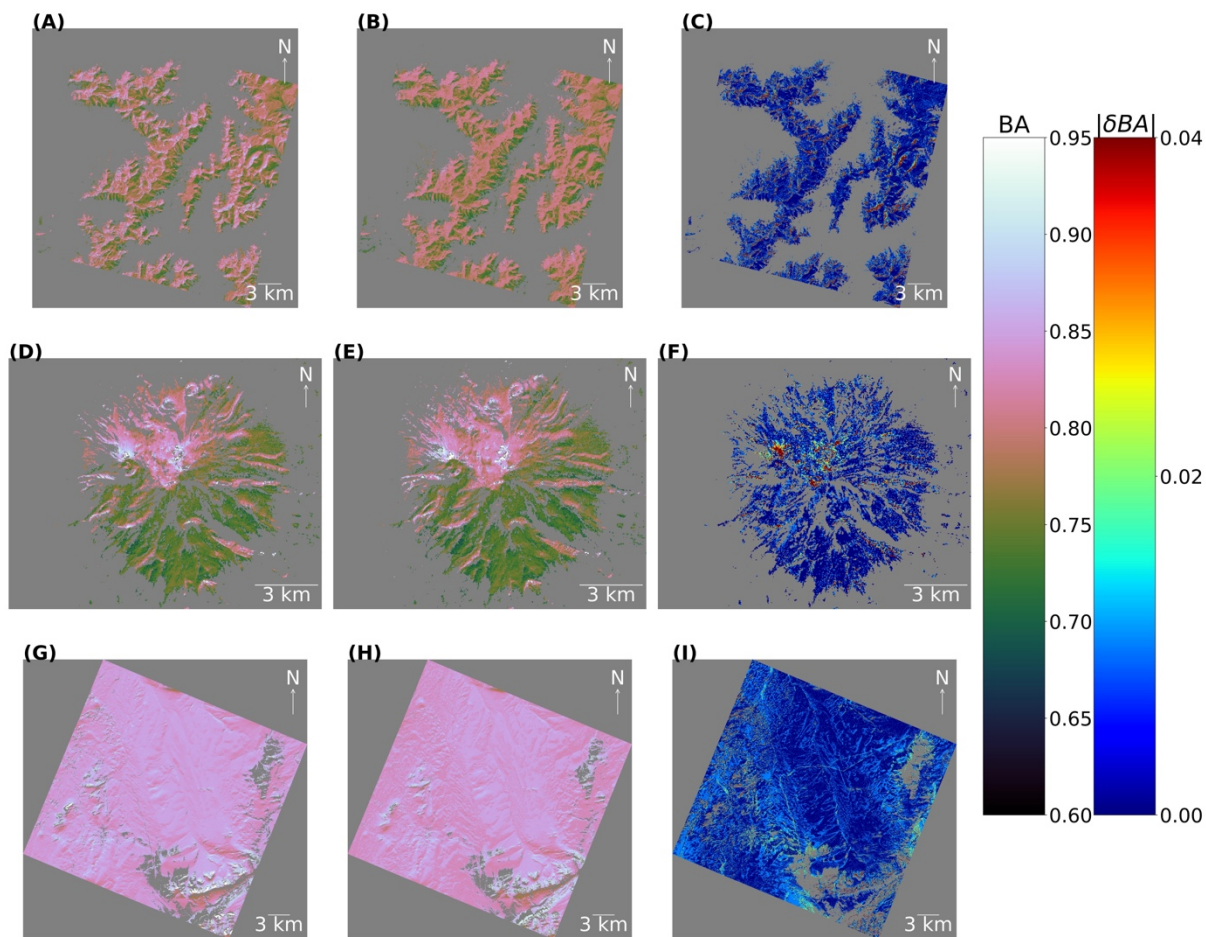
317

318 **Figure 6.** 2D Histogram plots showing absolute difference in SSA (left), broadband albedo
 319 (middle) and AOD (left) with respect to slope and aspect across the entire dataset. In this figure
 320 absolute difference is calculated as $|\text{Static} - \text{Radiance}|$. This is shown for the San Juan
 321 Mountains site (A,D,G), Shasta site (B,E,H), and Toolik site (C,F,I). The average solar zenith
 322 angle (θ_0) is shown for reference on each panel.

323

324 Putting this into spatial context (Figure 7), San Juan site had 37% of pixels (135.3 km²)
 325 with an absolute difference in BA ($|\delta\text{BA}| \geq 0.01$) and 14% pixels (49.9 km²) with $|\delta\text{BA}| \geq$

326 0.02. Shasta site had 30% of pixels (16.7 km²) with $|\delta BA| \geq 0.01$ and 9% pixels (5.1 km²)
 327 with $|\delta BA| \geq 0.02$. Toolik site had 40% of pixels (325.3 km²) with $|\delta BA| \geq 0.01$ and 8%
 328 pixels (66.6 km²) with $|\delta BA| \geq 0.02$.



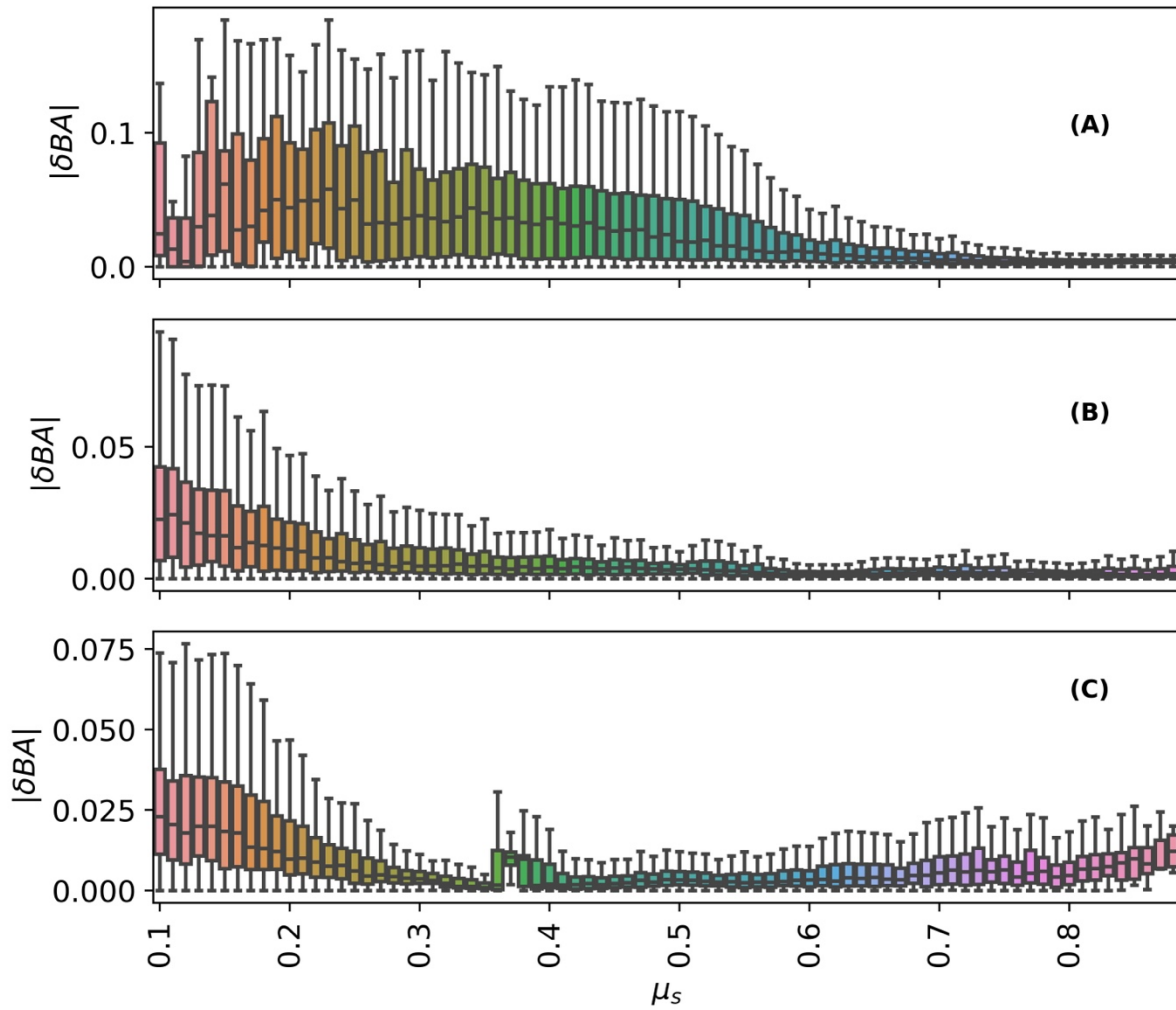
329
 330 **Figure 7.** Modelled broadband snow albedo (BA) for San Juan Mountains site (A-C), Shasta
 331 Mountain site (D-F), and Toolik site (G-I). Left column represents BA from static method,

332 middle column represents BA from radiance method, and right column represents absolute
333 difference in BA ($|\delta\text{BA}|$). Dark grey colour symbolizes data that is not a value.

334

335 Median $|\delta\text{BA}|$ for all sites with respect to μ_s general increased as μ_s approached zero
336 (Figure 8). For example, for the San Juan site, median $|\delta\text{BA}|$ ranged from 0.03 to 0.00 across
337 μ_s . For the Shasta and Toolik sites, median $|\delta\text{BA}|$ ranged from 0.02 to 0.00 across μ_s . This
338 relation was non-linear and depended on the site and illumination conditions. This analysis
339 demonstrates the levels of uncertainty potentially left in for retrievals relying on static, non-
340 coincident DEMs. This shows quantitatively the improvements to snow broadband albedo at
341 30 m scale by using radiance-based approach to be relatively small for well-lit slopes – on the
342 order 0-1%. While shaded slopes may have errors in snow broadband albedo on the order of
343 1-3%. Interestingly for the Toolik site, $|\delta\text{BA}|$ also increased as μ_s approached one.

344



345

346 **Figure 8.** Modelled absolute difference in broadband albedo ($|\delta BA| = |BA_{Static} - BA_{Radiance}|$)

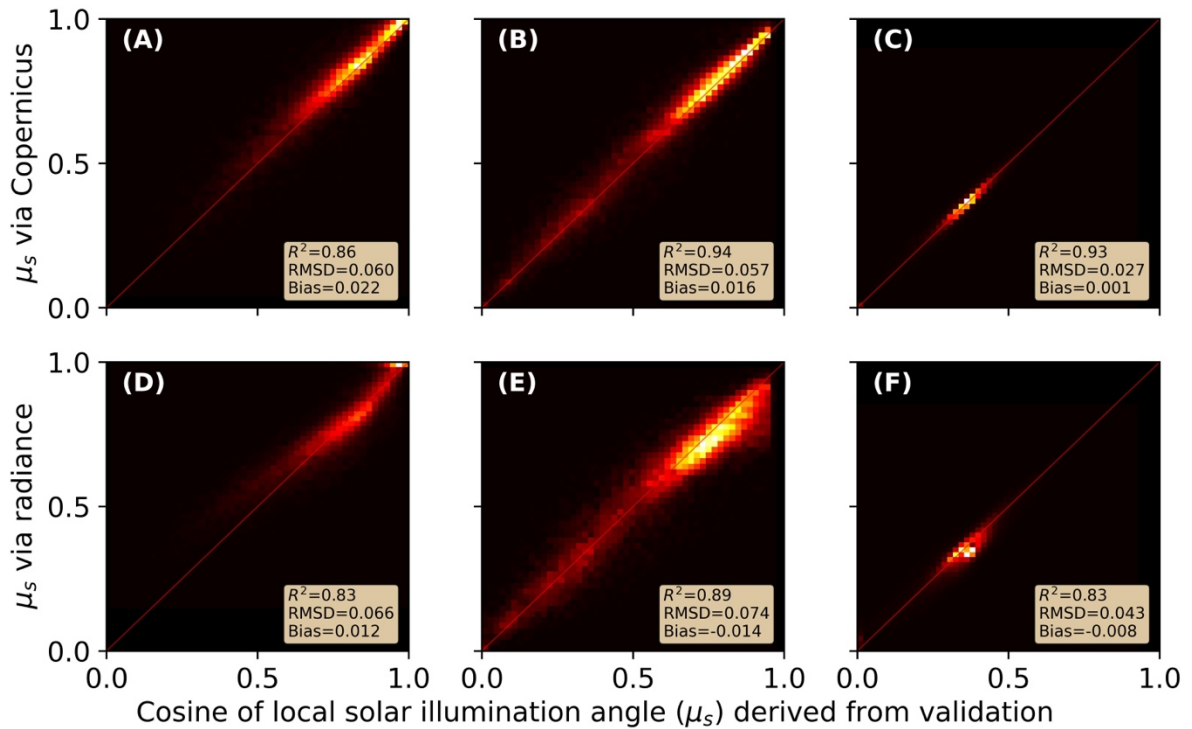
347 for San Juan (A), Shasta (B), and Toolik (C). Note these boxplots were created by rounding

348 μ_s to the nearest hundredth place.

349

350 **3.3 Comparing DEM and radiance derived μ_s**

351 At the 30 m pixel scale, Copernicus DEM derived μ_s had similar overall performance
352 to radiance derived μ_s (Figure 9), with Copernicus DEM derived μ_s having slightly higher
353 performance. For example, for the San Juan site, RMSD only varied by 0.006 between the
354 two methods. Similarly, the R^2 for Copernicus derived μ_s was 0.86, while the radiance
355 derived μ_s was slightly lower at 0.83. This similar overall performance was common amongst
356 the three sites. We found the average bias for radiance derived μ_s was generally closer to zero
357 (+/- 0.01), and did not show a strong negative or positive direction.



358

359 **Figure 9.** Comparing μ_s at 30 m pixel scale derived from radiance and Copernicus against high
360 resolution DEM for San Juan site (A,D), Shasta site (B,E), and Toolik site (C,F).

361

362 **4 Discussion**

363 **4.1 Radiance derived DEMs may replace coincident DEMs and contain information** 364 **related to surface roughness**

365 Derivative slope and aspect maps are prone to errors at 30 m spatial resolutions
366 (Dozier et al., 2022). This is relevant for derived snow products from upcoming missions
367 such as SBG and CHIME which will rely on topographic information to calculate optical
368 properties like snow albedo. These errors can be inherent to the DEM itself, or a product of
369 spatial and/or temporal misalignments (Carmon et al., 2023). Our modelled $|\delta BA|$ with
370 respect to the non-coincident DEM was similar to work by Donahue et al. (2023), who found
371 slightly higher uncertainties of broadband albedo (ranging from -10 to 10%) for their
372 investigation on Place Glacier, British Columbia, Canada. With the surface and roughness
373 undergoing dramatic change on glaciers throughout a given season, using this radiance-based
374 approach may be especially impactful for improving estimates over glaciers.

375 Snow surface roughness has long been a challenging issue in modelling snow
376 properties from space where the solar incidence angle at high spatial resolution for snow-on
377 DEM is not well known (Bair et al., 2022). Previous research found radiance derived μ_s from

378 airborne imaging spectroscopy showed a negative bias and postulated this could be due to
379 within-pixel topography, shadows, and surface roughness (Carmon et al., 2023). Since a bi-
380 directional reflectance function (BRDF) model was not used in their study, it then would be
381 plausible for the optimal μ_s to compensate for these effects. Interestingly when using a BRDF
382 model in our study (i.e., AART) and solving for aspect optimally (therefore informing μ_s , μ_v ,
383 and ξ) we did not find a strong bias – negative or positive. Although, we did not take surface
384 roughness measurements, and therefore do not know to the extent this impacted our study.
385 Within-pixel shadows, textures, and surface roughness remain difficult to validate, and we
386 were unable to achieve this in our study. Future work interested in further understanding this
387 radiance-based approach may investigate how such approaches interact with micro-scale
388 topography through ground measurements such as terrestrial and airborne lidar.

389

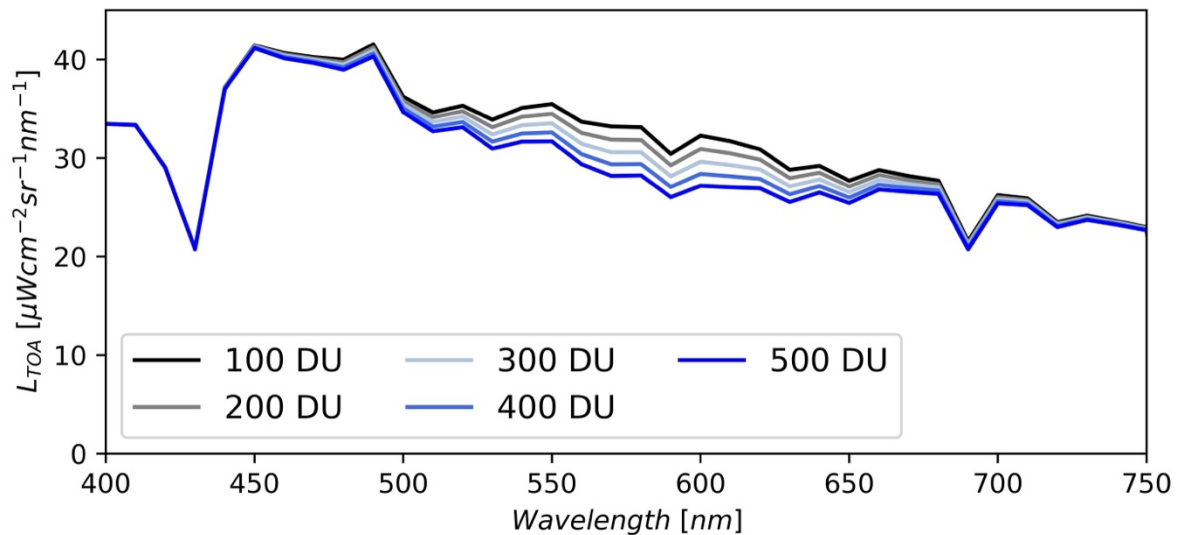
390 **4.2 Next steps in possibly improving this radiance-based approach**

391 While we solved for a few terrain parameters in this study we did not entirely remove
392 the use of the DEM from the radiance method. The elevation from global DEMs has a much
393 higher confidence than its derivative products (Dozier et al., 2022). Therefore, we used these
394 values to inform our atmospheric routine, as well as our shadow casting ray tracing module
395 (Wilder et al., 2024). Additionally, we used the method presented in Dozier (2022) for
396 estimating the sky view factor (V_Ω) based on nearby terrain and the pixel itself. This factor

397 could potentially be problematic but was cited as being not as impactful as μ_s in propagating
398 error (Dozier et al., 2022). Therefore, we elected to use V_Ω derived from the static Copernicus
399 DEM. However, this could be an area for future improvement, especially in very steep terrain
400 where V_Ω becomes small. It is not advised to attempt to add V_Ω directly into the optimization
401 routine presented in this study, as it is a function of pixel slope and aspect, and therefore,
402 altering V_Ω and aspect together would create invalid solutions. Finally, we used a static value
403 for slope derived from Copernicus DEM. The slope influences the μ_s term, but also
404 influences the passive radiation from nearby slopes. Ultimately, we concluded that aspect had
405 the largest impact on changing μ_s (Figure 1), as well as large RMSE reported in previous
406 work (Dozier et al., 2022; Donahue et al., 2023), and thus was the focus of our study. Caution
407 is advised in including both slope and aspect together, as non-unique solution space for μ_s
408 may cause the optimization outputs to become invalid. In summary, elevation, V_Ω , and slope
409 remain static in our current implementation. Future work may explore other algorithmic
410 choices to further remove, or improve, static DEM parameters.

411 Another consideration for improving this method is the inclusion of total column
412 ozone into the optimization. Previous research has been able to use TOA snow reflectance
413 data to retrieve reliable estimates of ozone (Kokhanovsky et al., 2021b). In our paper, we
414 elected for a simpler approach to first investigate the impacts of including terrain in the
415 optimization. In this paper we input a fixed ozone for the entire image based on coincident

416 Sentinel-5 measurements. However, it should be stated that ozone impacts a similar spectral
417 range to μ_s (Figure 10). It therefore may be beneficial to include ozone in the atmospheric
418 lookup-table (e.g., MODTRAN, libRadtran) to enable optimization of ozone as well. This
419 may be beneficial in building more realistic radiance-based methods.



420
421 **Figure 10.** Synthetic data showing change in magnitude of top of atmosphere radiance (L_{TOA})
422 with respect to changing total column ozone for fixed snow surface state variables modelled
423 with AART, and other fixed atmospheric state variables modelled with libRadtran. Reference
424 data is based on PRISMA image taken over southern Colorado. Note units of total column
425 ozone are shown in in Dobson Units (DU).

426

427 Finally, future studies should investigate including improvements to BRDF models of
428 snow (Mei et al., 2022). For example, recent work by Kokhanovsky et al. (2024) has
429 proposed the use of a two-layer model which may be especially useful for vertically
430 heterogenous snowpacks. Their method has been tested using EnMAP data and may easily be
431 transferable to other sensors. The current AART method we used in our paper does not
432 account for these layers, and instead assumes an optically thick, homogenous snowpack. To
433 validate both AART, the new layered approach, and future BRDF models, snow pit (i.e.,
434 vertical profile) measurements of SSA (e.g., Meloche et al., 2023) become essential in
435 ensuring models accurately account for diverse layering of snow.

436

437 **4.3 Big picture implications of the radiance-based approach**

438 This research responds to the objectives stated in “*Thriving on our changing planet: A*
439 *decadal strategy for Earth observation from space*”, to improve biogeophysical modelling at
440 scales driven by topography (National Academies of Science, Engineering, & Medicine,
441 2018), enabling more accurate snow property retrievals in the cryosphere under challenging
442 illumination conditions. Our work presented on solving terrain where DEM data are not
443 available, or reliable, may serve to accelerate improvements to satellite remote sensing tools
444 to monitor and model at both the regional global scale (Sturm et al., 2017), at a critical
445 juncture in time where northern latitudes are changing fast under a warming climate. This

446 includes Earth's glaciers, where radiance-based method may have the largest improvements
447 over static approaches. Our research is complimented by other recent works which show
448 promise in including terrain in the inversions (Bohn et al., 2024; Bohn et al., 2023; Bair et al.,
449 2024; Carmon et al., 2023)

450 We recommend additional coincident AVIRIS-NG flights with spaceborne imaging
451 spectroscopy datasets to further this work. As we have shown for the San Juan Mountains
452 site, for particularly warm days, images that are separated by longer than an hour may exhibit
453 drastically different SSA and liquid water content. As shown in this paper, this creates an
454 issue when trying to validate improvements to retrieval algorithms.

455

456 **5 Conclusion**

457 In this study we used existing PRISMA L1 TOA imagery to demonstrate the
458 improvements in modelling snow optical properties when explicitly modelling the terrain in
459 the inversion. This would especially be true for areas where the surface undergoes rapid
460 change, such as glaciers. This new method is especially useful for steep mountain terrain
461 and/or high latitudes where illumination conditions are suboptimal. The θ_0 (solar zenith
462 angle) was relatively low for the San Juan Mountains site in our study, and thus represents a
463 lower bound of the improvement in accuracy one could expect. This disparity was
464 demonstrated further for the Mount Shasta and Toolik sites when θ_0 was larger (i.e. a greater

465 difference in retrieved properties due to more challenging solar and sensor geometry). Even
466 for the relatively flat Toolik site, we showed that correctly accounting for incidence angles
467 can impact snow properties when θ_0 is large. Future work may look to build from this
468 radiance-based approach to enable better quantification of snow properties at scales impacted
469 by topography.

470

471 *Code Availability.* <https://github.com/cryogars/goshawk>

472 *Author contributions.* B.W. created the GOSHAWK algorithm and updates herein, decided
473 on experiment set-up, and performed the subsequent analysis, as well as being the main
474 article writer. J.M., J.E. and N.G. provided ideas, comments, and supervised the work.

475 *Competing interests.* The contact author has declared that neither they nor their co-authors
476 have any competing interests.

477 *Acknowledgements.* We acknowledge the Italian Space Agency (ASI) for providing us access
478 to PRISMA imagery and providing us the foundational data necessary for this research. We
479 thank Dr. McKenzie Skiles for aiding us in modelling the snow properties from AVIRIS-NG,
480 and for supplying the dataset.

481

482 *Financial support.* This research has been supported by FINESST Award – 21-EARTH21-
483 0249.

484

485 References

- 486 1. Bair, E. H., Dozier, J., Stern, C., LeWinter, A., Rittger, K., Savagian, A., Stilling, T.,
487 and Davis, R. E.: Divergence of apparent and intrinsic snow albedo over a season
488 at a sub-alpine site with implications for remote sensing, *The Cryosphere*, 16, 1765–
489 1778, <https://doi.org/10.5194/tc-16-1765-2022>, 2022.
- 490 2. Bair, E. H., Roberts, D. A., Thompson, D. R., Brodrick, P. G., Wilder, B. A., Bohn,
491 N., Crawford, C. J., Carmon, N., Vuyovich, C. M., & Dozier, J. Brief communication:
492 Not as dirty as they look, flawed airborne and satellite snow spectra. *EGUsphere*
493 [preprint], <https://doi.org/10.5194/egusphere-2024-1681>, 2024.
- 494 3. Bair, E. H., Stilling, T., and Dozier, J.: Snow property inversion from remote
495 sensing (SPIReS): A generalized multispectral unmixing approach with examples
496 from MODIS and Landsat 8 OLI, *IEEE Transactions on Geoscience and Remote*
497 *Sensing*, 59, 7270–7284, <https://doi.org/10.1109/TGRS.2020.3040328>, 2021.

- 498 4. Bohn, N., Painter, T. H., Thompson, D. R., Carmon, N., Susiluoto, J., Turmon, M. J.,
499 and Guanter, L.: Optimal estimation of snow and ice surface parameters from imaging
500 spectroscopy measurements, *Remote Sensing of Environment*, 264, 112613,
501 <https://doi.org/10.1016/j.rse.2021.112613>, 2021.
- 502 5. Bohn, N., Bair, E. H., Brodrick, P. G., Carmon, N., Green, R. O., Painter, T. H., and
503 Thompson, D. R.: Estimating dust on snow—application of a coupled atmosphere-
504 surface model to spaceborne EMIT imaging spectrometer data, in: *IGARSS 2023–*
505 *2023 IEEE International Geoscience and Remote Sensing Symposium*, 685–688,
506 IEEE, July 2023.
- 507 6. Bohn, N., Bair, E. H., Brodrick, P. G., Carmon, N., Green, R. O., Painter, T. H., and
508 Thompson, D. R.: The pitfalls of ignoring topography in snow retrievals: a case study
509 with EMIT, SSRN [preprint], <http://dx.doi.org/10.2139/ssrn.4671920>, 2024.
- 510 7. Carmon, N., Berk, A., Bohn, N., Brodrick, P. G., Dozier, J., Johnson, M., Miller, C.
511 E., Thompson, D. R., Turmon, M., Bachmann, C. M., Green, R. O., Eckert, R.,
512 Liggett, E., Nguyen, H., Ochoa, F., Okin, G. S., Samuels, R., Schimel, D., Song, J. J.,
513 and Susiluoto, J.: Shape from spectra, *Remote Sensing of Environment*, 288, 113497,
514 <https://doi.org/10.1016/j.rse.2023.113497>, 2023.

- 515 8. Cawse-Nicholson, K., Townsend, P. A., Schimel, D., Assiri, A. M., Blake, P. L.,
516 Buongiorno, M. F., Campbell, P., Carmon, N., Casey, K. A., Correa-Pabón, R. E.,
517 Dahlin, K. M., Dashti, H., Dennison, P. E., Dierssen, H., Erickson, A., Fisher, J. B.,
518 Frouin, R., Gatebe, C. K., Gholizadeh, H., Gierach, M., Glenn, N. F., Goodman, J. A.,
519 Griffith, D. M., Guild, L., Hakkenberg, C. R., Hochberg, E. J., Holmes, T. R. H., Hu,
520 C., Hulley, G., Huemmrich, K. F., Kudela, R. M., Kokaly, R. F., Lee, C. M., Martin,
521 R., Miller, C. E., Moses, W. J., Muller-Karger, F. E., Ortiz, J. D., Otis, D. B.,
522 Pahlevan, N., Painter, T. H., Pavlick, R., Poulter, B., Qi, Y., Realmuto, V. J., Roberts,
523 D., Schaepman, M. E., Schneider, F. D., Schwandner, F. M., Serbin, S. P.,
524 Shiklomanov, A. N., Stavros, E. N., Thompson, D. R., Torres-Perez, J. L., Turpie, K.
525 R., Tzortziou, M., Ustin, S., Yu, Q., Yusup, Y., Zhang, Q., and SBG Algorithms
526 Working Group: NASA's surface biology and geology designated observable: A
527 perspective on surface imaging algorithms, *Remote Sensing of Environment*, 257,
528 112349, <https://doi.org/10.1016/j.rse.2021.112349>, 2021.
- 529 9. Celesti, M., Rast, M., Adams, J., Boccia, V., Gascon, F., Isola, C., and Nieke, J.: The
530 Copernicus Hyperspectral Imaging Mission for the Environment (CHIME): Status
531 and Planning, in: *IGARSS 2022–2022 IEEE International Geoscience and Remote
532 Sensing Symposium*, 5011–5014, IEEE, July 2022.

- 533 10. Center for Snow and Avalanche Studies: Archival Data from Senator Beck Basin
534 Study Area, available at <https://snowstudies.org/archived-data/>, 2023.
- 535 11. Cogliati, S., Sarti, F., Chiarantini, L., Cosi, M., Lorusso, R., Lopinto, E., and
536 Colombo, R.: The PRISMA imaging spectroscopy mission: Overview and first
537 performance analysis, *Remote Sensing of Environment*, 262, 112499,
538 <https://doi.org/10.1016/j.rse.2021.112499>, 2021.
- 539 12. Dalcin, L., and Fang, Y. L. L.: mpi4py: Status update after 12 years of development,
540 *Computing in Science & Engineering*, 23(4), 47–54,
541 doi:10.1109/MCSE.2021.3083216, 2021.
- 542 13. Donahue, C., Skiles, S. M., and Hammonds, K.: Mapping liquid water content in
543 snow at the millimeter scale: an intercomparison of mixed-phase optical property
544 models using hyperspectral imaging and in situ measurements, *The Cryosphere*,
545 16(1), 43–59, <https://doi.org/10.5194/tc-16-43-2022>, 2022.
- 546 14. Donahue, C. P., Menounos, B., Viner, N., Skiles, S. M., Beffort, S., Denouden, T.,
547 and Heathfield, D.: Bridging the gap between airborne and spaceborne imaging
548 spectroscopy for mountain glacier surface property retrievals, *Remote Sensing of*
549 *Environment*, 299, 113849, <https://doi.org/10.1016/j.rse.2023.113849>, 2023.

- 550 15. Dozier, J.: Revisiting topographic horizons in the era of big data and parallel
551 computing, *IEEE Geoscience and Remote Sensing Letters*, 19, 1–5,
552 doi:10.1109/LGRS.2021.3125278, 2022.
- 553 16. Dozier, J., Bair, E. H., Baskaran, L., Brodrick, P. G., Carmon, N., Kokaly, R. F., and
554 Thompson, D. R.: Error and uncertainty degrade topographic corrections of remotely
555 sensed data, *Journal of Geophysical Research: Biogeosciences*, 127(11),
556 e2022JG007147, <https://doi.org/10.1029/2022JG007147>, 2022.
- 557 17. European Space Agency: Copernicus Global Digital Elevation Model [Dataset],
558 distributed by Open Topography, <https://doi.org/10.5069/G9028PQ>, 2021.
- 559 18. Green, R. O., Brodrick, P. G., Chapman, J. W., Eastwood, M., Geier, S., Helmlinger,
560 M., and Thorpe, A. K.: AVIRIS-NG L2 Surface Reflectance, Facility Instrument
561 Collection, V1, ORNL DAAC, Oak Ridge, Tennessee, USA, 2023.
- 562 19. Guanter, L., Kaufmann, H., Segl, K., Foerster, S., Rogass, C., Chabrillat, S., Kuester,
563 T., Hollstein, A., Rossner, G., Chlebek, C., Straif, C., Fischer, S., Schrader, S., Storch,
564 T., Heiden, U., Mueller, A., Bachmann, M., Mühle, H., Müller, R., Habermeyer, M.,
565 Ohndorf, A., Hill, J., Buddenbaum, H., Hostert, P., van der Linden, S., Leitão, P. J.,
566 Rabe, A., Doerffer, R., Krasemann, H., Xi, H., Mauser, W., Hank, T., Locherer, M.,
567 Rast, M., Staenz, K., and Sang, B.: The EnMAP spaceborne imaging spectroscopy

- 568 mission for earth observation, *Remote Sensing*, 7(7), 8830–8857,
569 <https://doi.org/10.3390/rs70708830>, 2015.
- 570 20. Hale, G. M. and Query, M. R.: Optical constants of water in the 200-nm to 200- μ m
571 wavelength region, *Applied Optics*, 12, 555–563,
572 <https://doi.org/10.1364/AO.12.000555>, 1973.
- 573 21. Kaspari, S., Skiles, M., Delaney, I., Dixon, D., and Painter, T. H.: Accelerated glacier
574 melt on Snow Dome, Mount Olympus, Washington, USA, due to deposition of black
575 carbon and mineral dust from wildfire, *Journal of Geophysical Research:*
576 *Atmospheres*, 120(7), 2793–2807, <https://doi.org/10.1002/2014JD022676>, 2015.
- 577 22. Kokhanovsky, A. A., and Zege, E. P.: Scattering optics of snow, *Applied Optics*,
578 43(7), 1589–1602, doi:10.1364/AO.43.001589, 2004.
- 579 23. Kokhanovsky, A. A.: The Broadband Albedo of Snow, *Frontiers in Environmental*
580 *Science*, 9, 757575, <https://doi.org/10.3389/fenvs.2021.757575>, 2021.
- 581 24. Kokhanovsky, A., Di Mauro, B., Garzonio, R., and Colombo, R.: Retrieval of dust
582 properties from spectral snow reflectance measurements, *Frontiers in Environmental*
583 *Science*, 9, 644551, <https://doi.org/10.3389/fenvs.2021.644551>, 2021a.
- 584 25. Kokhanovsky, A., Gascoin, S., Arnaud, L., and Picard, G.: Retrieval of snow albedo
585 and total ozone column from single-view MSI/S-2 spectral reflectance measurements

- 586 over Antarctica, Remote Sensing, 13(21), 4404, <https://doi.org/10.3390/rs13214404>,
- 587 2021b.
- 588 26. Kokhanovsky, A., Brell, M., Segl, K., Efremenko, D., Petkov, B., Bianchini, G.,
- 589 Stone, R., and Chabrillat, S.: The two-layered radiative transfer model for snow
- 590 reflectance and its application to remote sensing of the Antarctic snow surface from
- 591 space, Frontiers in Environmental Science, 12, 1416597,
- 592 <https://doi.org/10.3389/fenvs.2024.1416597>, 2024.
- 593 27. Leroux, C., and Fily, M.: Modeling the effect of sastrugi on snow reflectance, Journal
- 594 of Geophysical Research: Planets, 103(E11), 25779–25788,
- 595 <https://doi.org/10.1029/98JE00558>, 1998.
- 596
- 597 28. Malmros, J. K., Mernild, S. H., Wilson, R., Tagesson, T., and Fensholt, R.: Snow
- 598 cover and snow albedo changes in the central Andes of Chile and Argentina from
- 599 daily MODIS observations (2000–2016), Remote Sensing of Environment, 209, 240–
- 600 252, <https://doi.org/10.1016/j.rse.2018.02.072>, 2018.
- 601 29. Mayer, B., and Kylling, A.: The libRadtran software package for radiative transfer
- 602 calculations-description and examples of use, Atmospheric Chemistry and Physics,
- 603 5(7), 1855–1877, <https://doi.org/10.5194/acp-5-1855-2005>, 2005.

- 604 30. McKenzie, D.: Mountains in the Greenhouse: Climate Change and the Mountains of
605 the Western U.S.A., 10.1007/978-3-030-42432-9, 2020.
- 606 31. Mei, L., Rozanov, V., Jiao, Z., and Burrows, J. P.: A new snow bidirectional
607 reflectance distribution function model in spectral regions from UV to SWIR: Model
608 development and application to ground-based, aircraft and satellite observations,
609 ISPRS Journal of Photogrammetry and Remote Sensing, 188, 269–285,
610 <https://doi.org/10.1016/j.isprsjprs.2022.04.010>, 2022.
- 611 32. Meloche, J., Lemmetyinen, J., Meyer, K., Alabi, I., Vuyovich, C. M., Stuefer, S.,
612 Marshall, H., Durand, M., and Langlois, A.: SnowEx23 Laser Snow Microstructure
613 Specific Surface Area Data, Version 1 [Data Set], NASA National Snow and Ice Data
614 Center Distributed Active Archive Center, Boulder, Colorado,
615 USA, <https://doi.org/10.5067/BSEP59ADC6XN>, accessed 16 August 2024.
- 616 33. Miller, S. D., Wang, F., Burgess, A. B., Skiles, S. M., Rogers, M., and Painter, T. H.:
617 Satellite-based estimation of temporally resolved dust radiative forcing in snow cover,
618 Journal of Hydrometeorology, 17(7), 1999–2011, [https://doi.org/10.1175/JHM-D-15-](https://doi.org/10.1175/JHM-D-15-0150.1)
619 [0150.1](https://doi.org/10.1175/JHM-D-15-0150.1), 2016.
- 620 34. National Academies of Sciences, Engineering, and Medicine: Thriving on Our
621 Changing Planet: A Decadal Strategy for Earth Observation from Space, National
622 Academies Press, Washington, DC, 716 pp., doi:10.17226/24938, 2018.

623

624 35. O'Neel, S., Wilder, B., Keskinen, Z., Zikan, K. H., Enterkine, J., Filiano, D. L.,
625 Meehan, T., LeWinter, A., Deeb, E. J., Marshall, H.-P., & Adebisi, N.: Helicopter-
626 Borne Lidar to Resolve Snowpack Variability in Southwest Idaho, in: AGU Fall
627 Meeting Abstracts, Vol. 2022, C35E-0922, December 2022.

628 36. Painter, T. H., Seidel, F. C., Bryant, A. C., Skiles, S. M., and Rittger, K.: Imaging
629 spectroscopy of albedo and radiative forcing by light-absorbing impurities in
630 mountain snow, *Journal of Geophysical Research: Atmospheres*, 118(17), 9511–9523,
631 <https://doi.org/10.1002/jgrd.50520>, 2013.

632 37. Picard, G., Dumont, M., Lamare, M., Tuzet, F., Larue, F., Pirazzini, R., and Arnaud,
633 L.: Spectral albedo measurements over snow-covered slopes: theory and slope effect
634 corrections, *The Cryosphere*, 14, 1497–1517, [https://doi.org/10.5194/tc-14-1497-](https://doi.org/10.5194/tc-14-1497-2020)
635 [2020](https://doi.org/10.5194/tc-14-1497-2020), 2020.

636 38. Seidel, F. C., Rittger, K., Skiles, S. M., Molotch, N. P., and Painter, T. H.: Case study
637 of spatial and temporal variability of snow cover, grain size, albedo and radiative
638 forcing in the Sierra Nevada and Rocky Mountain snowpack derived from imaging
639 spectroscopy, *The Cryosphere*, 10(3), 1229–1244, [https://doi.org/10.5194/tc-10-1229-](https://doi.org/10.5194/tc-10-1229-2016)
640 [2016](https://doi.org/10.5194/tc-10-1229-2016), 2016.

- 641 39. Siirila-Woodburn, E. R., Rhoades, A. M., Hatchett, B. J., Huning, L. S., Szinai, J.,
642 Tague, C., Nico, P. S., Feldman, D. R., Jones, A. D., Collins, W. D., & Kaatz, L.: A
643 low-to-no snow future and its impacts on water resources in the western United
644 States, *Nature Reviews Earth & Environment*, 2(11), 800-819,
645 <https://doi.org/10.1038/s43017-021-00219-y> , 2021.
- 646 40. Skiles, S. M., & Painter, T.: Daily evolution in dust and black carbon content, snow
647 grain size, and snow albedo during snowmelt, Rocky Mountains, Colorado, *Journal of*
648 *Glaciology*, 63(237), 118-132, doi:10.1017/jog.2016.125, 2017.
- 649 41. Skiles, M. and Vuyovich, C. M.: SnowEx21 Senator Beck Basin and Grand Mesa, CO
650 AVIRIS-NG Surface Spectral Reflectance, Version 1 [Data Set], NASA National
651 Snow and Ice Data Center Distributed Active Archive Center, Boulder, Colorado
652 USA, <https://doi.org/10.5067/ZAI3M64WWN5V>, Date Accessed 02-09-2024.
- 653
- 654 42. Sturm, M., Goldstein, M. A., and Parr, C.: Water and life from snow: A trillion dollar
655 science question, *Water Resources Research*, 53(5), 3534-3544,
656 <https://doi.org/10.1002/2017WR020840>, 2017.

- 657 43. Tedesco, M., and Kokhanovsky, A. A.: The semi-analytical snow retrieval algorithm
658 and its application to MODIS data, Remote Sensing of Environment, 111(2-3), 228-
659 241, <https://doi.org/10.1016/j.rse.2007.02.036>, 2007.
- 660
- 661 44. U.S. Geological Survey: 3D Elevation Program 1-Meter Resolution Digital Elevation
662 Model (published 20200606), accessed June 1, 2023, at [https://www.usgs.gov/the-](https://www.usgs.gov/the-national-map-data-delivery)
663 [national-map-data-delivery](https://www.usgs.gov/the-national-map-data-delivery), 2019.
- 664 45. U.S. Geological Survey, 2022, 5 Meter Alaska Digital Elevation Models (DEMs) -
665 USGS National Map 3DEP Downloadable Data Collection, accessed June 1, 2023,
666 at <https://www.usgs.gov/the-national-map-data-delivery>, 2022.
- 667
- 668 46. Wang, W., Yang, K., Zhao, L., Zheng, Z., Lu, H., Mamtimin, A., Ding, B., Li, X.,
669 Zhao, L., Li, H., Che, T., & Moore, J. C. Characterizing surface albedo of shallow
670 fresh snow and its importance for snow ablation on the interior of the Tibetan
671 Plateau, Journal of Hydrometeorology, 21(4), 815-827, [https://doi.org/10.1175/JHM-](https://doi.org/10.1175/JHM-D-19-0193.1)
672 [D-19-0193.1](https://doi.org/10.1175/JHM-D-19-0193.1), 2020.

673

674 47. Warren, S. G., & Brandt, R. E. Optical constants of ice from the ultraviolet to the
675 microwave: A revised compilation, *Journal of Geophysical Research:*
676 *Atmospheres*, 113(D14), <https://doi.org/10.1029/2007JD009744>, 2008.

677

678 48. Wilder, B. A., Lee, C. M., Chlus, A., Marshall, H. P., Brandt, J., Kinoshita, A. M.,
679 Enterkine, J., Van Der Weide, T., & Glenn, N. F. Computationally Efficient Retrieval
680 of Snow Surface Properties From Spaceborne Imaging Spectroscopy Measurements
681 Through Dimensionality Reduction Using k-Means Spectral Clustering, *IEEE Journal*
682 *of Selected Topics in Applied Earth Observations and Remote Sensing*, vol. 17, pp.
683 8594-8605, doi:10.1109/JSTARS.2024.3386834, 2024.

684